Rotating spherical gap convection in the GeoFlow International Space Station (ISS) experiment

Florian Zaussinger [ORCID],[*] Peter Haun [ORCID], Peter S. B. Szabo, Vadim Travnikov,
Mustafa Al Kawwas, and Christoph Egbers
Brandenburg University of Technology Cottbus-Senftenberg,
Department of Aerodynamics and Fluid Mechanics, D-03046 Cottbus, Germany

Thermal convection in a rotating spherical gap is investigated using numerical simulations and compared with results of the GeoFlow ISS experiment. To induce convection, a radial buoyancy force field is established by using the dielectrophoretic effect from a high-frequency alternating electric field. Two heating sources are implemented. One source is a temperature difference across the gap and the other is the internal dielectric heating of the working fluid. To distinguish both heating sources a heating parameter, λ, is introduced that is varied together with the electric Rayleigh number, L, and Ekman number, $\text{Ek} \approx 10^{-3}$. The governing thermoelectro hydrodynamic equations are analyzed via a linear stability analysis and by three-dimensional numerical simulations. The results are compared with experimental data of the GeoFlow experiment which show that the threshold of convection and the occurrence of global columnar cells agreed with the theoretical predictions. In addition the observed fluid flow showed non-Gaussian characteristics which are described by the quasinormal approximation. The overall flow phenomena are based on polar plumes and equatorial confined columnar cells and in addition are influenced by internal dielectric heating.

I. INTRODUCTION

Internal heating processes in rotating spherical gaps are of great interest for geophysical and astrophysical applications. Important sources of internal heating are thermonuclear reactions (e.g., in stars), tidal heating, and gravitational heating (e.g., in moons and gas giants) or radioactive decay in terrestrial planets. Internal heating is an important component of hydrostatic equilibrium within stars which establishes the radiative pressure and determines the evolution of the entire body. For example, tidal heating is assumed to increase the heat flux of Jupiter's moon Europa. This leads to the possibility of fluid-filled basins and even of cryovulcanism [1]. The thermal energy release of planets is a key feature which can also be observed in the core of the Earth [2] or Venus [3].

Theoretical and numerical analysis of internal heating in spherical gap geometries has been intensively studied with particular focus on convection in the Earth's mantle [4,5]. However, large Prandtl numbers and large viscosity contrasts render it complicated to capture geophysically relevant convection in laboratory experiments. To overcome these limitations, results are based mainly on fluids with moderate Prandtl numbers (Pr < 200) and extrapolated to the geophysically relevant regime of Pr → ∞ [6–8].

So far, only a few convection experiments have been performed under the influence of internal heating. Limare *et al.* [9] studied highly viscous fluids over three orders of magnitudes of the

---

*florian.zaussinger@b-tu.de

063502-1

Rayleigh-Roberts number, Ra_H, and over two orders of magnitudes of Pr. Their work provided the first cross validation of convection with internal heating. Fourel *et al.* [10] improved this experiment by introducing a compositional gradient to study heterogeneities assumed to be in the Earth's lower mantle [11]. The interaction between the two internally heated layers provide a vast variety of convective patterns. Internal heating is not only interesting from an academic point of view, it is also used in several industrial applications such as microwave ovens, mixed convection devices for cooking, to melt glass, process food or even to dry items.

Internal heating-induced convection in the spherical gap geometry has been studied by Zaussinger *et al.* [12] using numerical simulations and experimentally measured data from the GeoFlow IIc experiment [13]. Experimental and numerical interferograms of GeoFlow provided information to test properties of the electrohydrodynamical (EHD) model. They also observed a thermal plumelike distribution and a parabolic mean temperature profile in the radial direction. However, an analysis of rotational effects and a temperature difference between the inner and outer shell were not included in the study. Nonetheless, both of these properties are important for convection in stellar interiors [14] and in planets [15]. An extension to the cylindrical geometry was performed by Travis and Olson [16] that studied a temperature difference across the annulus in the presence of a dielectric internal heating source. A large parameter regime was investigated focusing on fluid flow that was characterized by Ra_H. A scaling law in planar geometry for mixed heating was studied by Vilella and Deschamps [17]. However, these results cannot be directly transferred to the EHD model where the sign of the temperature gradient may change the direction of the buoyancy term.

Thermo-EHD establishes a force field with the dielectrophoretic acceleration as consequence. This acceleration can be used to drive and control fluid motion. The pioneering work on the EHD model in a rectangular cavity was published by Roberts [18] and Turnbull [19] in the late 1960s. Both investigated the stability of the conductive state even in the absence of buoyancy which is an important limitation for space applications. Since then, this theoretical work has been extended and tested by laboratory experiments, see Refs. [20–22]. Heat transfer in a planar EHD system under microgravity conditions was investigated by Yoshikawa *et al.* [23] and Fogaing *et al.* [24]. They compared the heat flux of Rayleigh-Bénard (RB) convection with EHD convection for a large range of Prandtl numbers and explained that differences are due to thermal perturbations induced by the electric field. EHD convection in a spherical capacitor was studied without rotation [12,25] and finally, in the AtmoFlow experiment, with rotation [26]. The GeoFlow experiment was performed over eight years (from 2008 to 2016) on the ISS. The first mission, GeoFlow I, used a silicon oil, M5, to investigate the dynamics of an idealized Earth's core [27]. The second mission, GeoFlow II, operated on the ISS from 2011 to 2018 and studied mantellike dynamics of an idealized Earth with 1-Nonanol as a working fluid. It operated over three scientific campaigns: GeoFlows IIa, IIb, and IIc. However, only the GeoFlow IIc campaign operated with a frame rate of 10 Hz. All other campaigns used 1 Hz or less.

The analogy between the EHD model instability and the RB model instability is violated by two processes: first, the *thermoelectric feedback*, which generates perturbation components in the electric gravity [28]. This feedback is a result of the Gauss equation which couples the temperature-dependent permittivity and the electric field. The second process is *dielectric heating*, a result of the rotation of molecules under a quickly alternating electric field. While dielectric heating occurs in many working fluids, it has not yet been investigated in detail in the EHD models. Dielectric heating is not yet fully controllable and can lead to unpredictable hot spots and damage [29,30].

The main objective of this work is the investigation of convection due to the dielectrophoretic force in a rotating spherical gap with the focus on the influence of dielectric heating. This paper is an extension of the authors' previous work presented by Zaussinger *et al.* [12] which investigated the nonrotating case. For this purpose, the higher statistical moments of numerical simulations are analyzed to reveal the influence of rotation and internal heating. The findings are then compared with the experimental data of the GeoFlow II mission.
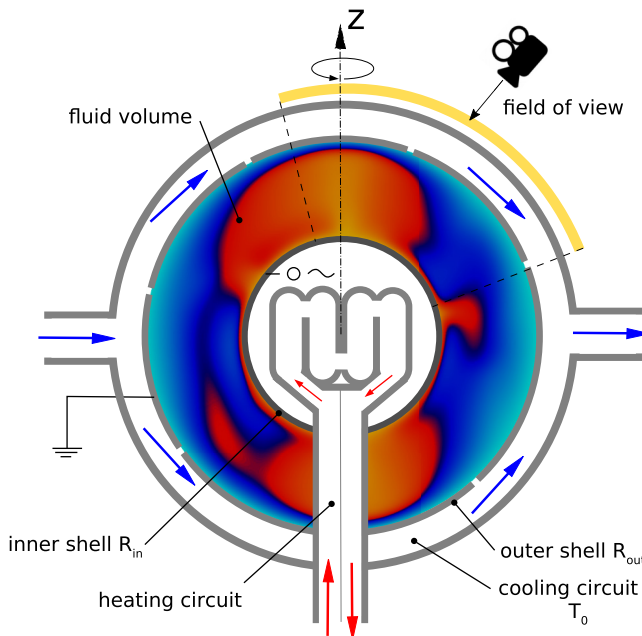
FIG. 1. Schematic cross section of the GeoFlow experimental setup showing a numerically calculated temperature distribution over the gap.

This paper is outlined as follows: The general EHD model and governing equations for the rotating spherical gap are presented in Sec. II, whereas the GeoFlow experiment and numerical methods are described in Sec. III. Analytic results and a detailed statistical description of the fluid flow in the rotating spherical gap are given in Secs. IV and V, respectively. This includes a comparison between numerical simulations and experimental interferograms. A critical discussion of the results and some concluding remarks are given at the end.

II. MODEL FORMULATION

A spherical capacitor with gap width $d = R_{\text{out}} - R_{\text{in}}$, with the same physical specifications as the GeoFlow experiment is filled with a dielectric fluid. The temperature field is imposed (a) with a temperature difference between the inner and outer shell with $\Delta T = T_{\text{in}} - T_0 > 0$ and (b) by an internal heat source which includes dielectric heating. A cross-section schematic of the experiment is shown in Fig. 1. We assume an electrically linear quasielectrostatic field acting on an incompressible dielectric fluid such that the net force on each dipole is given by the *Kelvin polarization force density* $\mathbf{F} = (\epsilon - \epsilon_0)\mathbf{E} \cdot \nabla\mathbf{E}$, where ϵ is the temperature dependent permittivity, ϵ_0 the vacuum permittivity, and $\boldsymbol{E}$ the electric field.

Thus, the electric *Korteweg-Helmholtz force density* describes the force acting on the fluid and is valid for the given assumptions according to Refs. [12,28,31,32] and written as

$$\mathbf{F}_{\text{KH}} = \rho_f \mathbf{E} - \frac{1}{2}|\mathbf{E}|^2 \nabla\epsilon + \nabla\left(\frac{1}{2}\rho\frac{\partial\epsilon}{\partial\rho}|\mathbf{E}|^2\right). \tag{1}$$

where ρ is the density. The first term on the right-hand side of the equation represents the Coulomb force, the second term the dielectrophoretic force $\mathbf{F}_{\text{DEP}}$, and the last term the electrostrictive force defining the electrostrictive pressure. A detailed description of the derivation of $\mathbf{F}_{\text{KH}}$ is given in Melcher [33].

The fluid is considered to not carry free charges, so that $\rho_f = 0$ and the Coulomb force vanishes. The electrostrictive pressure will be combined with the hydrodynamic pressure in the incompressible momentum equation.

An alternating electric field with potential $\Phi(t) = 2V_{\text{rms}} \cos(2\pi ft)$ is applied at one electrode where f is the ac frequency and V_{rms} the root-mean-square capacitor voltage. This model of the electrostatic equilibrium is justified for $\tau_e^{-1} \ll f \ll d/c$, where τ_e is the charge relaxation time and c is the speed of light [18].

The dielectric loss is given by the power dissipation per unit mass, written as

$$H = \frac{2\pi f\epsilon \tan \delta |\mathbf{E}|^2}{c_p \rho}, \tag{2}$$

where $\tan \delta$ is the ratio between the imaginary and the real part of the permittivity and called the dielectric loss factor [34] and c_p is the specific heat capacity at constant pressure.

A. Governing equations

The equations describing the fluid flow are based on the Oberbeck-Boussinesq approximation (OBA). The OBA assumes low expansion rates with temperature $\alpha \Delta T \ll 1$, where α is the thermal expansion coefficient with a low thermoelectric parameter $e\Delta T \ll 1$, where $e = -\frac{1}{\epsilon}\frac{\partial \epsilon}{\partial T}$ is the thermal permittivity coefficient that decreases with increasing temperature [28]. Under these conditions, the OBA is valid for density $\rho = \rho_0[1 - \alpha(T - T_0)]$ and permittivity $\epsilon = \epsilon_0\epsilon_r[1 - e(T - T_0)]$, where ϵ_r is the relative permittivity at reference temperature T_0.

The problem can now be described with the Navier-Stokes equation by considering the above formulations as

$$\frac{\partial \mathbf{u}}{\partial t} + (\mathbf{u} \cdot \nabla)\mathbf{u} = -\frac{1}{\rho_0}\nabla p - \frac{1}{2\rho_0}|\mathbf{E}|^2\nabla\epsilon - 2\mathbf{\Omega} \times \mathbf{u} - \frac{\rho}{\rho_0}\mathbf{\Omega} \times (\mathbf{\Omega} \times \mathbf{r}) + \nu\nabla^2\mathbf{u}, \tag{3}$$

where $\mathbf{u}$ is the velocity, p the pressure, $\mathbf{\Omega}$ the rotation vector, $\mathbf{r}$ the position vector, and ν the kinematic viscosity. The temperature equation is

$$\frac{\partial T}{\partial t} + (\mathbf{u} \cdot \nabla)T = \kappa_T\nabla^2 T + H, \tag{4}$$

where T is the temperature and κ_T the thermal diffusivity. Mass conservation is given by the continuity equation $\nabla \cdot \mathbf{u} = 0$. The nonuniform electric field and the thermoelectric feedback is calculated via the Gauss equation [23],

$$\nabla \cdot (\epsilon \mathbf{E}) = 0. \tag{5}$$

Following Eq. (5) above, the direction of the $\mathbf{F}_{\text{DEP}}$ is toward the permittivity gradient and is therefore collinear with the electrostatic energy stored in the fluid [28].

We now derive the dimensionless governing equations which are obtained by applying the scaling length $r = r^* d$, velocity $\mathbf{u} = \mathbf{u}^* \kappa_T/d$, time $t = t^* d^2/\kappa_T$, electric field $\mathbf{E} = \mathbf{E}^* V_{\text{rms}}/d$, temperature difference $T = T^*\Delta T + T_0$, and pressure $p = p^* \rho_0\kappa_T^2/d^2$, where the superscript * denotes the value as a dimensionless quantity. The fluid and electric properties are considered constant and taken at the outer shell. Thus, we obtain the dimensionless Navier-Stokes equation,

$$\text{Pr}^{-1}\left[\frac{\partial \mathbf{u}^*}{\partial t^*} + (\mathbf{u}^* \cdot \nabla)\mathbf{u}^*\right] = -\text{Pr}^{-1}\nabla p^* + \nabla^2\mathbf{u}^* - \frac{1}{4}\text{B} \cdot \Gamma \cdot \text{L} \cdot T^* \cdot \nabla|\mathbf{E}^*|^2$$

$$- \text{Ek}^{-1}\mathbf{e}_z \times \mathbf{u}^* + \text{L} \cdot \text{Fr} \cdot T^* r\sin\theta \, \mathbf{s}, \tag{6}$$

where $\text{Pr} = \nu/\kappa_T$ is the Prandtl number, $B = e/\alpha$ the ratio of both thermal expansion coefficients, $\text{Ek} = \nu/(2\Omega d^2)$ the Ekman number, r the radial distance, θ the poloidal direction, $\mathbf{s}$ is the unit vector in the equatorial plane, $\text{Fr} = \Omega^2 d/|g_{e,R_{\text{out}}}|$ is the Froude number measuring the relative strength of

TABLE I. Dimensionless parameter range of the GeoFlow experiment. Parameters with asterisks are defined in the Appendix.

Dimensionless parameter	Value
Ekman number (Ek)	2.64×10^{-3}–7.62×10^{-3}
Froude number (Fr)	5.1×10^{-2}–2.66
Prandtl number (Pr)	1.24×10^2–1.75×10^2
Electric Rayleigh number (L)	3.73×10^2–1.59×10^5
Dielectric loss parameter (C_T)*	9.06×10^3–2.27×10^6
Convective parameter (C_E)*	2.02×10^{-7}–3.54×10^{-6}
Expansion ratio (B)	11.20–12.40
Heating parameter (λ)	0.16–60

the centrifugal and the electric gravity force [35], and

$$L = \alpha \Delta T |g_{e,R_{\text{out}}}| d^3/(\nu \kappa_T) \tag{7}$$

is the electric Rayleigh number given as a ratio of buoyancy to heat diffusion and viscous dissipation. The expression of the electric gravity, g_e, is suitable for substituting gravitational acceleration with the assumption derived in Appendix by neglecting the fluctuation of $\mathbf{E}$ and the electric feedback effect. Hence g_e is defined as

$$g_e(r) = -2V_{\text{rms}}^2 \frac{\epsilon_0 \epsilon_r}{\rho_0} \frac{R_{\text{in}}^2 R_{\text{out}}^2}{(R_{\text{out}} - R_{\text{in}})^2} \frac{1}{r^5} \tag{8}$$

at $r = R_{\text{out}}$. Values of defined dimensionless parameters for the GeoFlow experiment are summarized in Table I.

The dimensionless equation for temperature is

$$\frac{\partial T^*}{\partial t^*} + (\mathbf{u}^* \cdot \nabla) T^* = \nabla^2 T^* + \frac{C_T}{B \, \Gamma \, L} |\mathbf{E}^*|^2. \tag{9}$$

We now introduce the heating parameter, λ, written as

$$\lambda = \frac{1}{2} \frac{C_T}{B \Gamma L}, \tag{10}$$

which is used to quantify the heating source in the system. The heating parameter is in fact a result of the energy balance in terms of Nusselt numbers, Nu_{in} and Nu_{out}, evaluated at the inner and outer shells, respectively. Their relationship is written as

$$\text{Nu}_{\text{in}} - \text{Nu}_{\text{out}} + 2\lambda \int_V \mathbf{E}_0^2 \, dV = 0 \quad \text{for } \lambda < 1, \tag{11}$$

$$-\text{Nu}_{\text{in}} - \text{Nu}_{\text{out}} + 2\lambda \int_V \mathbf{E}_0^2 \, dV = 0 \quad \text{for } \lambda > 1. \tag{12}$$

The strength of the internal heating is measured by λ, where $\lambda > 1$ indicates strong internal heating and $\lambda < 1$ indicates weak internal heating. For $\lambda = 1$ internal heating increases the fluid's temperature inside the spherical gap geometry until the heat flux through the surfaces is balanced with the internal heating rate. When $\lambda > 1$, the temperature difference across the gap does not contribute significantly to the global energy transport and results in a parabolic mean temperature profile. Figure 2(a) provides an overview of different thermal profiles for various internal heating parameters.

After introducing the internal heating parameter one need also to define a quantitative parameter for the strength of convection. To investigate the flow we therefore define a further dimensionless
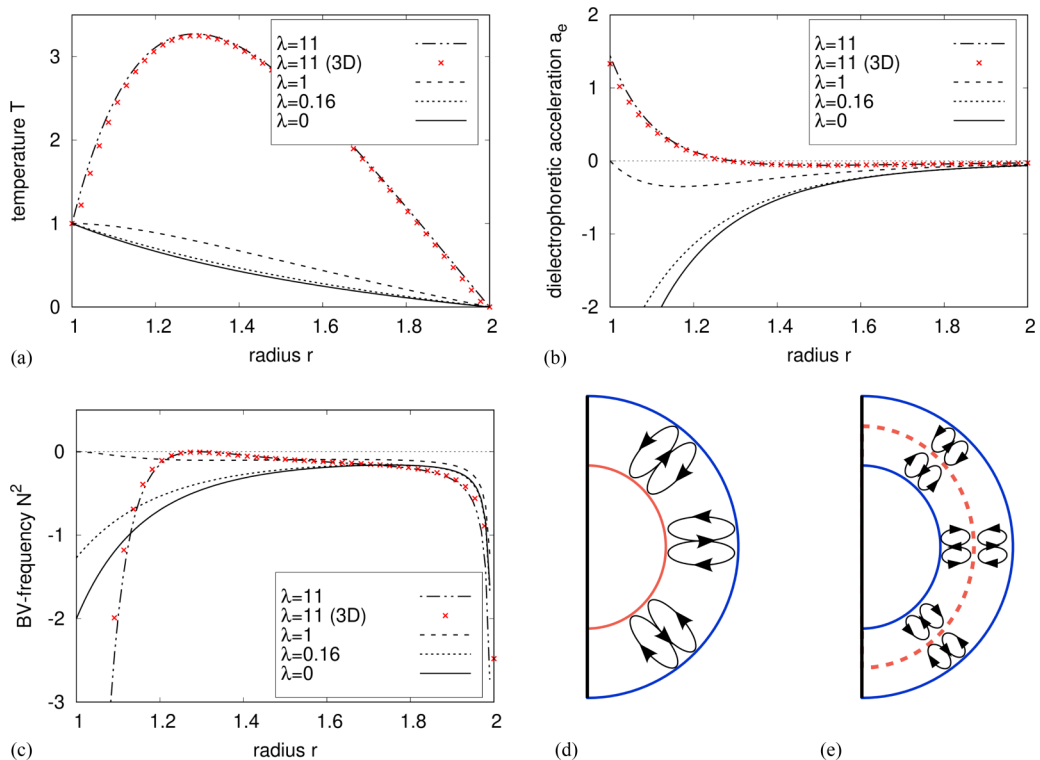
FIG. 2. Analytic solutions for (a) radial temperature distribution, (b) dielectrophoretic acceleration, and (c) Brunt-Väisälä frequency for varying λ in conductive and nonrotating case for $\eta = 0.5$. Red crosses ("x") present solutions for a three-dimensional numerical simulation with $\lambda = 11$. Values for λ are chosen according to the GeoFlow experiment. (d) Sketch of convection in the spherical gap geometry when $N^2 < 0$ in the complete gap and $\lambda < 1$). (e) Sketch of layered convection in the spherical gap geometry where $N^2 \geqslant 0$ at the middle of the gap and $N^2 < 0$ elsewhere with $\lambda > 1$.

quantity the dielectrophoretic acceleration, $\mathbf{a}_e^*$, written as

$$\mathbf{a}_e^* = -\tfrac{1}{2}|\mathbf{E}|^2 \boldsymbol{\nabla}\epsilon / \left[d^3 / \left(V_{\mathrm{rms}}^2 \epsilon_0 \epsilon_r\right)\right], \tag{13}$$

which is used to provide an indication of how strong an infinitesimal fluid element is forced at a certain location in the gap. In the next sections dimensionless parameters are used and the asterisk are omitted.

III. METHODS

A. The GeoFlow experiment

The GeoFlow experiment on the ISS consists of a concentric spherical gap capacitor that is used for the investigation of thermal convection. The experimental system has a gap width of 0.0135 m, with an outer radius of $R_{\mathrm{out}} = 0.027$ m resulting in an aspect ratio of $\eta = 0.5$ ($\Gamma = 0.25$). Figure 1 shows a numerically calculated temperature distribution over the spherical gap. Two external temperature controlled fluid circuits established a temperature difference of $0.4\,\mathrm{K} \leqslant \Delta T \leqslant 9.5\,\mathrm{K}$ between both shells. To induce a dielectrophoretic forcing and hence a radial buoyancy force a fast alternating electric field is applied. The strength of the force can be controlled by the applied thermal forcing and the amplitude of the electric field. The electric field can be adjusted between 1273 V and 4596 V to study a variety of convection phenomena. To account for rotational forcing, the sphere is

able to rotate with three different angular velocities, Ω, namely with $\Omega = 0.05$, 5, or 10 rad/s. The dielectric loss of the working fluid, 1-Nonanol, is caused by the high electric field frequency which generates dielectric internal heating and is also investigated.

The GeoFlow experiment can simulate three different rotation rates, five voltages $V_{\rm rms}$ and eight temperature differences, where two reference temperatures, T_0, are measured at the outer shell. These input properties define 240 experimental points (EP). The present study includes 160 EPs, summarized in Table I, which presents the full parameter range. However, the weakly rotating case of $\Omega = 0.05$ rad/s with Ek ≈ 1 and Fr $< 10^{-4}$ is excluded in this study. All numerical results presented are based on EPs defined in the GeoFlow *Experimental Scientific Requirements* (ESR) document. A set of eight temperature differences is called a "run" and can be set for a sequential increase of voltages and rotation rates. Five runs are grouped into four clusters. An overview of the each cluster is given in Figs. 4(a)–4(d).

The model formulation in Sec. II suggests that the electric Rayleigh number cannot be chosen independently from C_T as this would lead to inhomogeneous distributed sequences in the λ-L plane, where the heating parameter λ [see Eq. (10)] more intuitively parametrizes the influence of internal heating than C_T. Hence, for the analysis of the dynamics, we group the EPs in such a way that electric Rayleigh number varies only within a predicted dynamical range depending on the critical electric Rayleigh number L_c, but the heating parameter λ remains as strong as possible.

The EPs were visualized by a Wollaston Shearing Interferometry (WSI) system which measures the gradient of the refractive index [13,36]. While the refractive index gradient varies with the thermal distribution within the spherical gap, certain fringe patterns can be observed where the thermal gradient changes the (temperature-dependent) refractive index of the fluid. For example, single convective cells appear as butterfly patterns and sheetlike flows appear as parallel lines [see Fig. 5(c)]. Unfortunately, other visualizations of convective flow could not be performed for ISS safety reasons. The recording plane of the camera of the WSI is mounted at a meridional angle of $\theta = 30°$ with the North Pole located at $\theta = 0°$. Thus, the recorded interferograms cover a range of $88°$, ranging from $\theta = -14°$ to $\theta = 74°$, see Fig. 1. From a series of images it is possible to reconstruct the entire northern hemisphere. While the temporal resolution of the images enables a satisfactory analysis for the laminar flow regime, it causes imprecise reconstructions in the transient and turbulent regimes. To overcome these restrictions, only single interferograms are analyzed.

B. Numerical methods

The governing equations are studied using two methods: (a) a linear stability analysis which provides the critical electric Rayleigh numbers L_c and threshold values of the convective onset and (b) three-dimensional large eddy simulations (LES) and interferograms calculated with the software package OpenFoam. The numerical simulations provide the temperature and electric field for the statistical evaluation which are compared with interferograms. For the linear stability analysis, a pseudospectral numerical method is used to solve the dimensionless governing equations [37]. Here the velocity field is decomposed into poloidal and toroidal potentials ψ_1 and ψ_1,

$$\mathbf{u} = \nabla \times \nabla \times (\psi_1 \mathbf{e}_r) + \nabla \times (\psi_2 \mathbf{e}_r), \tag{14}$$

obeying the continuity equation. By using the pseudospectral method and applying $\nabla \times \nabla \times$ and $\nabla \times$ to Eq. (6) (which separates the potentials), one can solve the hydrodynamic equations with a high accuracy in the spherical geometry. This results in a fourth-order equation for the potential ψ_1 and a second-order equation for the potential ψ_2. The critical electric Rayleigh numbers, L_c, are calculated using linearized equations [38]. The corresponding eigenvalue problem is solved by direct numerical integration, where the spectrum is analyzed for growth rates $\sigma = 0$.

For the three-dimensional numerical simulations an incompressible, second-order finite volume, transient buoyancy solver of OpenFoam 4.1 is used which is expanded to include the nonuniform electric field as derived in Appendix. In addition, the solver includes the source terms for the

dielectric heating, H, in the temperature equations and the volumetric body force, F_{DEP}, in momentum equation.

The boundary condition for velocity is no-slip, in a moving reference frame, and Dirichlet for temperature. To mimic the GeoFlow experiment in all aspects, the experimental time scales are set consistent with Zaussinger *et al.* [12]. This included the heating-up periods and the idle periods between each EP. The electric field is defined as a negative gradient of the electric potential and is calculated via the Gauss equation, $\nabla \cdot (\epsilon \nabla \Phi) = 0$, by taking the electrical fluctuations and thermoelectric feedback effect into account. The boundary condition of the electric potential is set at the outer shell with $\Phi = V_{\text{rms}}$ and $\Phi = 0V$ at the inner shell.

The mesh of the spherical gap is generated by radially extruding a spherical two-dimensional (2D) surface grid with 40.950 faces to 1.843.290 honeycomb shaped cells in 3D with a radial resolution of 45 cells. The dimensionless wall distance y^+ is smaller than 0.2 and corresponds to a mesh resolution of at least five cells in the viscous boundary layer. The OpenFoam "Pimple" algorithm solves subsequently the LES model with top-hat filtered versions of Eqs. (3)–(5). The filter width is the cube root volume of each cell. VanDriest damping in distance to the boundary layer ensures that the "dynamic k" turbulence model is applied only in the bulk flow [39].

C. Statistical evaluation

The statistical interpretation is based on snapshots of temperature and dielectrophoretic force. These snapshots are averaged over shells (θ, ϕ) of equidistant radii and over 30 time stamps providing 300 s of the fully developed flow. Hence, the calculated profiles of the first four statistical moments are functions of the radius.

Turbulence and intermittency lead to rare, but intense peaks in the temperature field. As a result, in such intermittent systems especially the higher-order moments depart significantly from the Gaussian distribution. In particular, the evaluation of the third and the fourth statistical moments provide information of rarely occurring events. For convective processes these events are commonly related to thermal plumes.

The first statistical moment, $\langle T \rangle$, is the mean thermal distribution. Temperature fluctuations are described by the variance which is the second statistical moment $\langle T'^2 \rangle$.

An asymmetry of the temperature distribution around the mean value $\langle T \rangle$ is parametrized by the temperature skewness $\langle S \rangle = \langle T'^3 \rangle / (\langle T'^2 \rangle)^{3/2}$. Large positive values of S characterize locally higher values of T which cover a smaller surface area. Hence, the values deviate further from the mean value than locally lower values. The same holds for large negative values of S for cold areas embedded in a hot surrounding [40]. In particular, for $S > 0$ the fluid flow is dominated by strong uprising thermals and for $S < 0$ by strong downdrafts, respectively.

Intermittency is evaluated by the kurtosis (flatness) $\langle K \rangle = \langle T'^4 \rangle / (\langle T'^2 \rangle)^2$. The kurtosis provides a scale of a certain "tailedness" and describes rarely occurring and very spiky events in intermittent systems [41]. For the present study, high values of the kurtosis indicate localized regions with plumes of large magnitude, and large areas with slow ascending and descending flow. However, the direction of the fluid flow in the plumes is given by the sign of the skewness.

The higher statistical moments are very sensitive to rare events. They are indicating in this particular case thermal structures with steep gradients.

IV. BASE FLOW AND THRESHOLD OF CONVECTION

We assume that the toroidal and poloidal components of $\mathbf{E}_1(r, \theta, \phi)$ in the conductive case have only small contributions to the initial electric field $\mathbf{E}_0(r)$. This justifies the assumption of a one-dimensional electric field $\mathbf{E}(r)$. The Gauss equation and the temperature equation are solved analytically for a constant permittivity with the electric field equation presented in Eq. (A6) and the
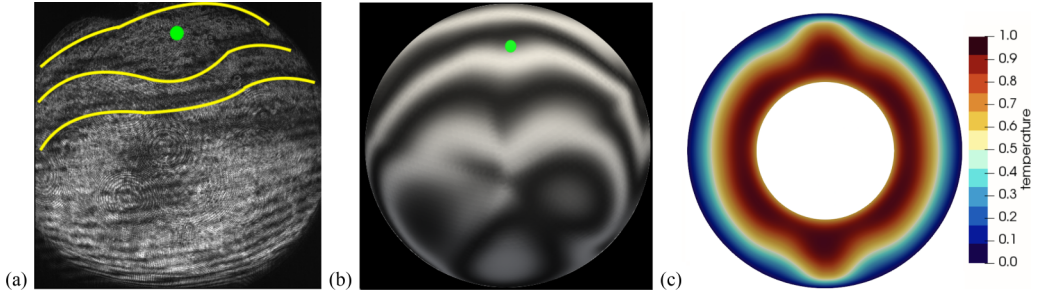
FIG. 3. (a) experimental interferogram for Ek $= 5.2 \times 10^{-3}$ and $\lambda = 1$ for the conductive case. The base flow structures are outlined in yellow, with a sinusoidal distortion around the North Pole labeled with a green dot. The equator is in the lower part of the interferogram. (b) Numerical interferograms with the same parameters evaluated by a three-dimensional simulation. (c) Vertical plane of the temperature distribution through both poles.

temperature condition imposed in the form of

$$T(r) = -\frac{\eta}{1-\eta} + \frac{\eta}{(1-\eta)^2}\frac{1}{r} - \lambda\left[\frac{\eta}{(1-\eta)^2} - \frac{\eta(1+\eta)}{(1-\eta)^3}\frac{1}{r} + \frac{\eta^2}{(1-\eta)^4}\frac{1}{r^2}\right]. \tag{15}$$

This solution is the sum of the base temperature profile, $-\frac{\eta}{1-\eta} + \frac{\eta}{(1-\eta)^2}\frac{1}{r}$, and the contribution from the dielectric heating whose amplitude is λ.

1. Thermal profile

To investigate the base state of the experiment the conductive reference case of run "C20" ($\lambda = 11$) of the GeoFlow experiment is studied. This includes a range of values for the heating parameter, λ, to study the transition state ($\lambda = 1$) where internal and external heating is balanced, where internal heating is absent ($\lambda = 0$), and the smallest achievable value of the GeoFlow experiment ($\lambda = 0.16$). The analytical solutions of the temperature fields are shown in Fig. 2(a) together with the 3D numerical simulation for $\lambda = 11$ indicated by red crosses which present good agreement with the corresponding analytic solution. In the case where $\lambda < 1$, the internal heating is negligible and convection is triggered by ΔT. For $\lambda > 1$, the temperature field reaches a maximum at the inner shell at $r_{max} = 4\lambda/(1 + 3\lambda)$. In this case, the stability of the system depends on the interaction of the signs of the dielectrophoretic acceleration that is influenced by the temperature gradient. In the limiting case of $\lambda \gg 1$, the temperature converged to the maximum at approximately $r_{max} = 4/3$. For $\lambda \leqslant 1$, the maximum is always found at the inner shell with $r_{max} = 1$ and radius ratio $\eta = 0.5$. In the absence of rotation (Fr $= 0$) the isothermal surfaces take the form of concentric spheroids with radially dependent temperature distributions. However, for small voltages ($V_{rms} \leqslant 2121$ V), the Fr exceeds 0.5 and influences the thermal stratification [42].

In the presence of rotation a two-dimensional axisymmetric and equatorially symmetric steady base flow appears ($u_r, u_\theta, 0$). Warm fluid is displaced radially outward at the poles whereas cold fluid is transported inward close to the equatorial plane. When the observed flow exhibits such complex motion it cannot be solved analytically and has to be calculated numerically. A meridional flow is observed in a two-cell structure at Ek, Fr $\sim 10^{-3}$ where the temperature maximum is found in the gap for internal heating. However, at the poles there is a radial shift of the temperature maxima toward the outer shell [see Fig. 3(c)]. The base flow of the GeoFlow experiment shows a plumelike structure at the North Pole and wave distortions in the conductive steady state case. Figure 3(a) shows these structures with yellow lines. Numerical simulations and the corresponding numerically evaluated interferograms agreed well with the experimental observation, see Figs. 3(b) and 3(c). However, the numerical reconstruction of the interferograms shows a more pronounced fringe

pattern in the polar region. This, however, is a result of the differently calibrated interferometry unit that is used for the calculation.

2. Dielectrophoretic acceleration and buoyancy

In the conductive case the electric field follows the solution of $\mathbf{E}_0 \sim r^{-2}$ [see Eq. (A6)] where $\mathbf{E}_0$ is independent of λ. However, the dielectrophoretic acceleration $\mathbf{a}_e$ [obtained from Eq. (A2)] depends on λ and is strictly negative for $\lambda \leqslant 1$ [see Fig. 2(b)]. The dielectrophoretic acceleration can be calculated by the analytic solution of the temperature by using the OBA for the permittivity and the scaling relation $\beta = e \, \Delta T \, \epsilon_r$ the radial component of the dielectrophoretic acceleration is written as

$$a_e(r) = -\frac{1}{2}|\mathbf{E}_0|^2 \frac{d\,\epsilon}{d\,r} = -\frac{1}{2}\left(\frac{1}{\Gamma}\frac{1}{r^2}\right)^2 \beta \left[\frac{2}{r^2} + \lambda\left(\frac{6}{r^2} - \frac{8}{r^3}\right)\right] \tag{16}$$

for $\eta = 0.5$. Figure 2(b) depicts the radial component of the dielectrophoretic acceleration $a_e(r)$ for four different values of λ. For $a_e(r) < 0$, the sign of dielectrophoretic acceleration is negative and points radially inward toward the center of the spherical gap. This generates an induced force field comparable to the gravitational force field. However, for $\lambda > 1$, the dielectrophoretic acceleration changes its sign at $r_{\max}$ and can separate the spherical gap into two layers. A deeper insight into the stability of the thermal stratification is given by the Brunt-Väisälä (BV) frequency written as

$$N^2 = -\frac{a_e}{T}\frac{d\,T}{d\,r}. \tag{17}$$

An unstable fluid column is observed at $\lambda > 1$ where $N^2 < 0$, except at a region around the temperature maximum where $N^2 = 0$. The absence of buoyancy indicates two convectively unstable layers separated by a stable conductive interface, see Fig. 2(e). While the strong forcing of the dielectrophoretic acceleration is present in the lower shell, a long-time separation is unlikely and a fully mixed spherical gap is expected. When $\lambda < 1$ the entire fluid column is unstable and presents convective patterns reminiscent of an RB cell see Fig. 2(d).

In the rotating case the threshold of the convective onset is characterized by the destabilization of the base flow which is observed by the interferometry unit when the fringe pattern is distorted. For all four clusters [see Figs. 4(a)–4(d)] the onset of convection is observed within a margin of ± 177 V. However, for $L \sim L_c$, ambiguous interferograms are recorded in which a clear distinction between the base flow and the convective flow was not possible.

V. THREE-DIMENSIONAL SIMULATIONS AND COMPARISON WITH THE GEOFLOW EXPERIMENT

The Geoflow experiment provides only interferograms which show the radially averaged temperature distribution of the gap and not the flow. Thus, we use three-dimensional simulations to reconstruct the flow field and temperature. Numerical results are used to explain the interferograms and to evaluate how significantly the dielectric heating parameter, λ, influences the flow and temperature distribution.

Of 160 analyzed EPs we find 22 (14%) with $\lambda < 1$ and 138 (86%) with $\lambda \geqslant 1$ with a mean value of $\lambda = 5.6$ and median of $\lambda = 2.1$. The minimum value is $\lambda = 0.16$ at $V_{\mathrm{rms}} = 1273$ V with temperature difference of $\Delta T = 9.5$ K. The maximum value of $\lambda = 60$ is found for the highest available voltage $V_{\mathrm{rms}} = 4596$ V and the lowest temperature difference $\Delta T = 0.4$ K. All cases with $\lambda < 1$ are found at low voltage ($V_{\mathrm{rms}} = 1273$ V) in combination with high temperature differences $\Delta T > 3$ K. All 160 EPs of the GeoFlow experiment are grouped into four clusters with respect to four Ekman numbers and two Prandtl numbers, (Ek $= 7.6 \times 10^{-3}$, Pr $= 176$), (Ek $= 5.2 \times 10^{-3}$, Pr $= 125$), (Ek $= 3.8 \times 10^{-3}$, Pr $= 176$), and (Ek $= 2.6 \times 10^{-3}$, Pr $= 125$). Figures 4(a)–4(d) visualize these clusters. To provide an adequate overview, the experimentally recorded interferograms are analyzed

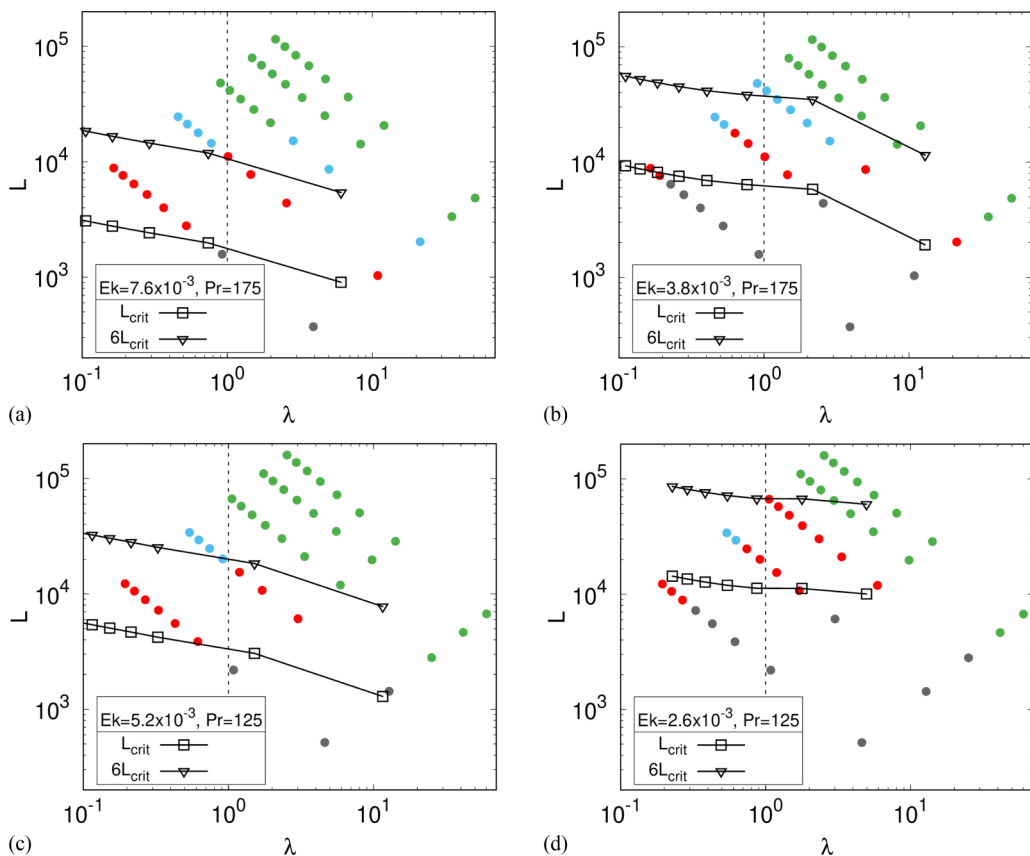FIG. 4. Experimental points (EP) of the GeoFlow experiment in the λ-L plane for (a) Ek $= 7.6 \times 10^{-3}$, Pr $= 175$; (b) Ek $= 3.8 \times 10^{-3}$, Pr $= 175$; (c) Ek $= 5.2 \times 10^{-3}$, Pr $= 125$; and (d) Ek $= 2.6 \times 10^{-3}$, Pr $= 125$. Dark gray dots represent the conductive cases, red dots the columnar flows, blue dots the transition and green dots the turbulent cases. Black lines with $\square$ symbols mark the onset of convection, and with $\triangledown$ symbols the transition to the turbulent regime.

and categorized into several separate cases where the conductive states are colored in dark gray, columnar flows in red, transitional cases with remnants of columnar cells in blue and turbulent cases in green. The black line with $\square$ symbols represents the result of linear stability analysis with the critical Rayleigh number L_c, whereas the black line with $\triangledown$ symbols separates the weakly nonlinear regime from the transitional regime. The vertical dashed line represents the transition between convection where the temperature difference across the gap dominates the energy transport ($\lambda < 1$) and the internal heating dominates convection ($\lambda > 1$). In the subsequent section, the dynamics of rotating convection are investigated in more detail, regarding the influence of the heating parameter, λ, the electric Rayleigh number, L. The Prandtl number, Pr, and the Ekman number, Ek, vary only little in the experiment which makes it difficult to deduce meaningful influences on the fluid flow.

A. Weakly nonlinear regime

The weakly nonlinear regime is defined as the region where $L \lesssim 6\,L_c$ [43]. In this regime, the dynamics follow approximately the Proudman-Taylor (PT) theorem with $\frac{\partial \mathbf{u}}{\partial z} \approx \mathbf{0}$, where z denotes any line parallel to the z axis of rotation. Within this regime, the pressure force is balanced by the Coriolis force and leads to the formation of columnar cells which are aligned with the rotation axis
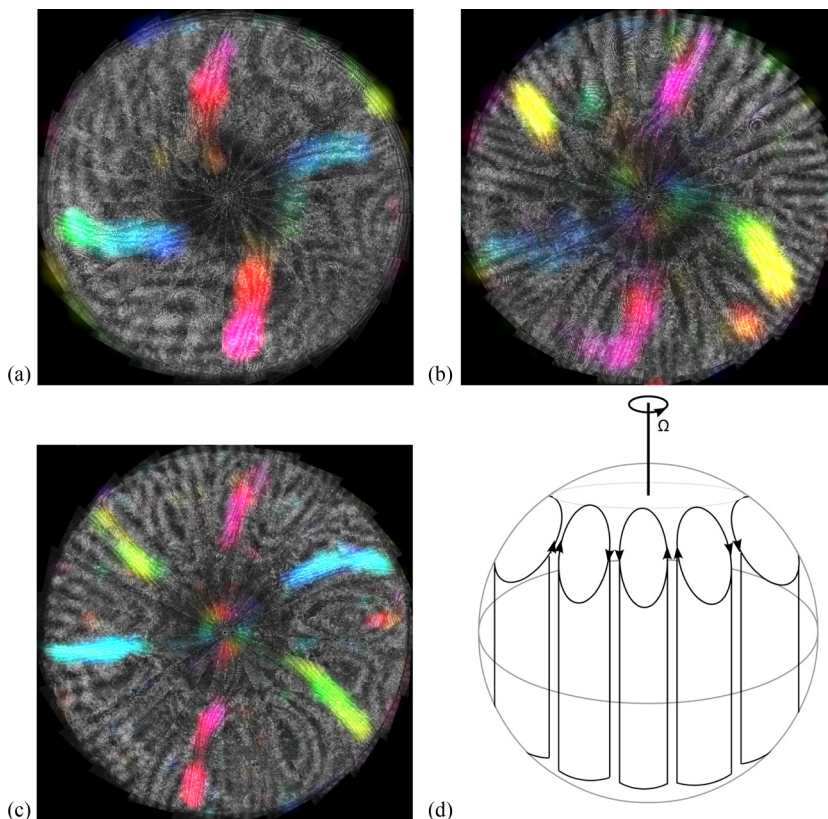
FIG. 5. Columnar cells visualized by automatic pattern recognition, Zaussinger *et al.* [13]. The North Pole is located in the center and the equator at the outline. The colors refer to angles of identified fringe lines. (a) Spiraling columnar cells with $m = 4$ for $L = 8849$, Ek $= 7.6 \times 10^{-3}$, and $\lambda = 0.16$, (b) slightly spiraling columnar cells with $m = 5$ for $L = 7217$, Ek $= 5.2 \times 10^{-3}$, and $\lambda = 0.33$, (c) almost straight cells with $m = 6$ for $L = 12243$, Ek $= 5.2 \times 10^{-3}$, and $\lambda = 0.19$. Animations of all three cases are available as Supplemental Material files in Refs. [46–48]. (d) Sketch of columnar cells aligned with the rotation axis in the spherical shell.

and confined by the tangent to the inner sphere. Spirals occur for impermeable boundaries that tilt the columnar cells. These spirals are well known to occur for moderate Prandtl numbers and are visible in equatorial cuts of the corresponding numerical simulations (see Ref. [44]). The azimuthal wave numbers of the columnar cells are estimated using $m \sim \text{Ek}^{-1/3}$ [43,45] which corresponds to $m \sim 5$–7 for the parameter range of the GeoFlow experiment. Deviations from the theoretical values by one wave number can be explained by the influence of the supply shaft at the South Pole of the experiment (Fig. 1) and by the nonuniform buoyancy force. The regime in which columnar cells occur is delimited by the 6 L_c criterion, but does not depend on λ, Ek, or Pr.

Figure 5 shows columnar cells with a fourfold, fivefold, and sixfold symmetry. The corresponding experimental points are labeled with wave numbers in Figs. 4(a)–4(d). The starlike structures show steep thermal upwelling and large down-welling regions. Columnar cells can be identified as butterfly patterns which are observed in the upper part of Fig. 5(c). Spiral structures are found for cases as presented in Fig. 5(a) and 5(b).

1. Thermal profile

To analyze the fluid flow in the weakly nonlinear regime of GeoFlow we carried out numerical simulations with the parameters of two representative runs, with $L/L_c = 1.15$ ("C17") and

$L/L_c = 2.25$ ("C20"). Both runs differ only in the high voltage and cover fairly wide ranges in the heating parameter. Figure 4(a) shows these EPs, where $L/L_c = 1.15$ and $\lambda = 10$ is labeled as "1," $L/L_c = 1.15$ and $\lambda = 0.5$ is labeled as "2," $L/L_c = 2.25$ and $\lambda = 2.5$ is labeled as "3," and $L/L_c = 2.25$ and $\lambda = 0.16$ is labeled as "4." In all four cases the mean temperature profiles $\langle T \rangle$ do not show strong convective mixing in the bulk of the fluid [see Fig. 6(a)]. This is to be expected as the onset of convection is close to the threshold. When convective mixing appears, the profiles in the bulk flatten and the boundary layers compress toward the shell's boundaries.

According to the PT theorem columnar cells are expected in the rotating case. Consistent to this, our numerical simulations found columnar cells with wave numbers between $m = 4$ and $m = 8$ which are visible for both heating scenarios, as shown in Figs. 6(g) and 6(h). When $\lambda < 1$, the variance is significantly smaller and shows peaks in the vicinity of the boundaries caused by homogeneously thermalized, rising and/or falling plumes, see Fig. 6(b). The maxima of the thermal fluctuations is observed between $1.5 < r < 1.8$ and coincides with the heating activities in the interior of the polar plumes.

Figures 6(c) and 6(d) shows the averaged skewness and kurtosis in the radial direction. The skewness has a flat profile with values $|S| \leqslant \sqrt{2}$ and $K \leqslant 3$ for $1 < r < 1.3$. This region can be described by the quasinormal approximation where the realizability condition [49], $K > 1 + S^2$, provides an upper boundary for the skewness. Furthermore, the observed values of S and K are in good agreement with the elevator model of convective cells which shows a similar sub-Gaussian behavior ($1 < K < 3$). In the upper half of the gap ($r > 1.5$) we found $|S| \geqslant \sqrt{2}$ and $K > 3$. The positive sign of S and the increase in S and K originates from the centrifugal force. In GeoFlow, the centrifugal force leads to the formation of two dominant up-flows in polar regions.

2. Stability and N^2

The dielectrophoretic acceleration shows behavior similar to that of the conductive case (see Fig. 2). For $\lambda < 1$, the dielectrophoretic acceleration is strictly negative due to the negative radial temperature gradient. A change of sign in the dielectrophoretic acceleration is found for $\lambda > 1$. However, this did not influence the global stability. The BV frequency N^2 is always negative or zero which indicates convective mixing over the entire gap [see Fig. 6(e) and 6(f)]. Far from the boundaries a layering such as two convectively layers separated by a diffusive interface [see Fig. 2(e)] was not observed.

B. Transitional regime for $\lambda \leqslant 1$

For $L > 6 L_c$ the regular columnar cells disperse and the flow becomes more turbulent. Fig. 10(a) shows a representative EP where the columnar cells are visible, but not regular any more. Consequently, Gastine *et al.* [50] denoted this parameter regime as the "transitional regime." A set of five representative EPs were analyzed for $L > 6 L_c$ and $\lambda < 1$ and are shown in Fig. 4(a) as four blue circles and the red circle inside the region defined as "set 1."

1. Thermal profile

The electric Rayleigh number L is in the range of $1.1 \times 10^4 \leqslant L \leqslant 2.4 \times 10^4$ which corresponds to values slightly above the weakly nonlinear regime with heating parameters between $0.16 \leqslant \lambda \leqslant 1.01$. The averaged temperature field $\langle T \rangle$ and the corresponding variance $\langle T'^2 \rangle$ are shown in Figs. 7(a) and 7(b). For the entire parameter range, the mean temperature shows a well mixed bulk between $r = 1.1$ and $r = 1.7$.

Just as in the weakly nonlinear regime, the centrifugal force leads to a non-Gaussian thermal distribution for $r > 1.5$. Polar plumes are detached toward the upper boundary to form a cell covering the entire gap. Columnar cells confined by the tangent cylinder are only weakly connected to the outer shell. This results in a broad upper boundary layer, but an increase in S and K due to polar plumes, see Fig. 7(c) and 7(d). The skewness is bounded by $\sqrt{2}$ for $r < 1.75$ due to columnar
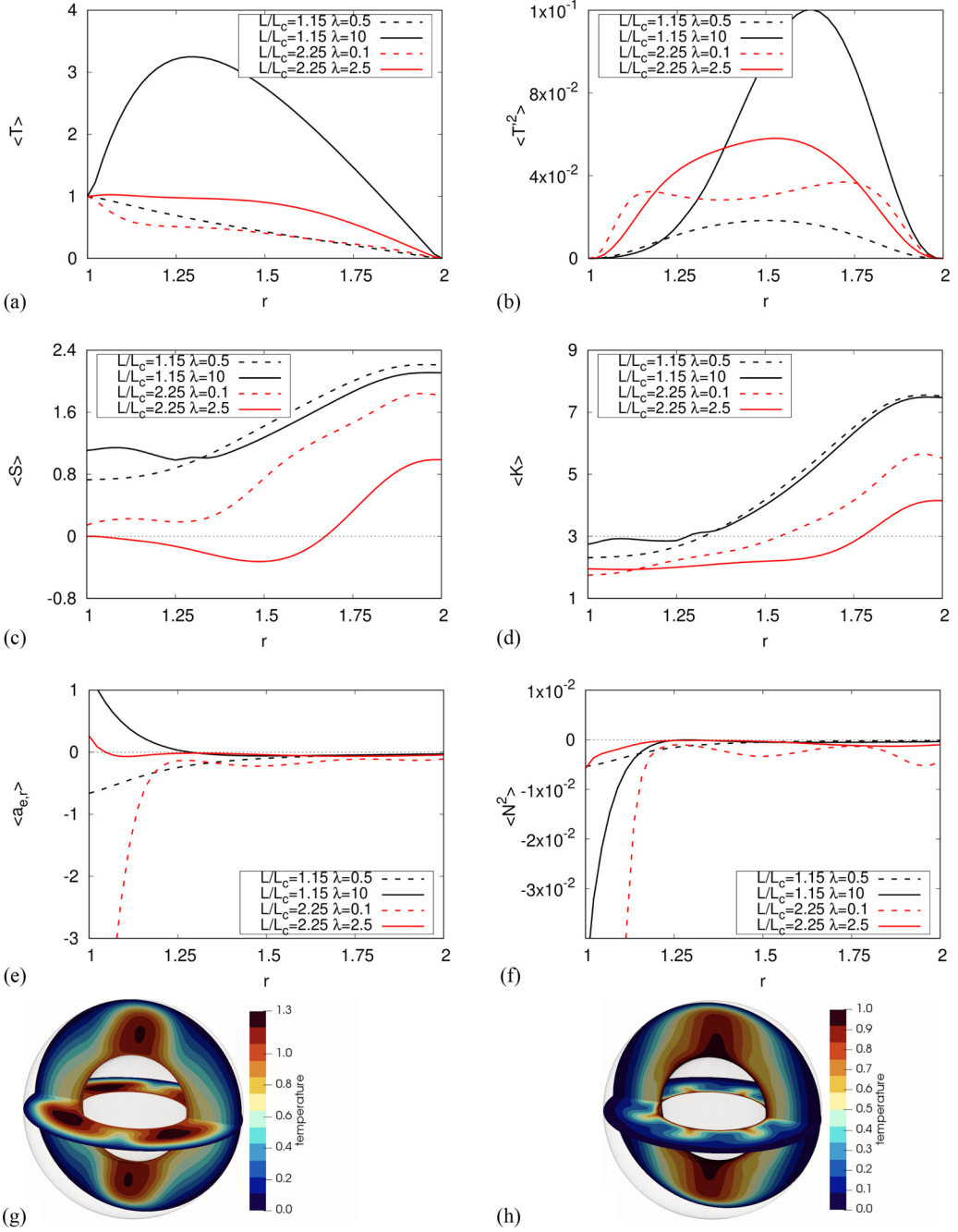
FIG. 6. Averaged thermal properties for simulations with $L/L_c = 1.15$ (black) and $L/L_c = 2.25$ (red), for $\lambda < 1$ and $\lambda > 1$, respectively. (a) The mean temperature, (b) the temperature variance, (c) the skewness of the temperature, (d) the kurtosis of temperature, (e) the dielectrophoretic acceleration, (f) the Brunt-Väisälä frequency, (g) the a 3D simulation for $L/L_c = 2.25$ and $\lambda = 2.5$, and (h) a 3D simulation for $L/L_c = 1.15$ and $\lambda = 0.16$.
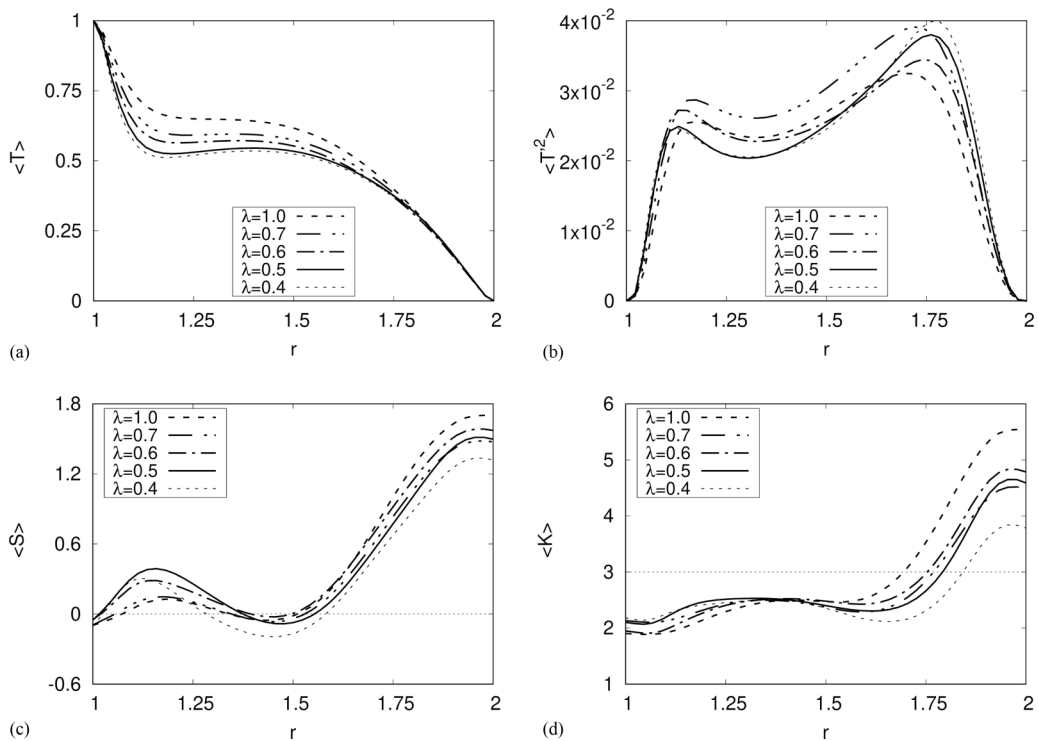
FIG. 7. Averaged (a) temperature, (b) temperature variance, (c) skewness of temperature, and (d) kurtosis of temperature for $\lambda \leqslant 1$ and $1.4 \times 10^4 < L < 2.4 \times 10^4$.

cells and this leads to a sub-Gaussian ($K \sim 2$) distribution. In contrast to the weakly nonlinear regime, this region is more strongly mixed due to higher convective fluxes.

2. Stability and N^2

Figure 8(a) shows an additional effect of the centrifugal force. A steep gradient exhibits in the dielectrophoretic acceleration, $\mathbf{a}_e$, at the equatorial region close to the inner shell with $r < 1.1$. The steep gradients at the inner shell are caused by the boundary layers formed by the columnar cells. As shown in Fig. 8(a), the dielectrophoretic acceleration as well as the BV frequency nearly vanish for $r > 1.1$. The confinement of columnar cells by the tangent cylinder and the resulting stable stratification above $r = 1.6$ reduce the thermal gradients and hence the dielectrophoretic acceleration. In summary, the upper boundary regions of the midlatitudes are nearly adiabatically stratified with $N^2 \sim 0$. In the polar regions, the dielectrophoretic acceleration and the BV frequency are nonzero at the outer shell which agree with the results shown in Fig. 2(c). The mean dielectrophoretic acceleration shows a small peak around $r = 1.8$ which is due to the boundary layer. The horizontal components of $\mathbf{a}_e$ does not contribute to the dynamics [see Fig. 8(b) and 8(c)]. The absolute values are two to three orders of magnitudes smaller than the radial component which justifies the use of Eqs. (A8) and (A9) for the parameter range investigated.

C. Transitional regime for $\lambda > 1$

A set of seven representative EPs with $2.0 \times 10^3 < L < 3.5 \times 10^4$ are analyzed for the parameter regime $\lambda > 1$, $\mathrm{Pr} = 175$, and $\mathrm{Ek} = 3.8 \times 10^{-3}$. The heating parameters range between $1.2 < \lambda \leqslant 21$ and are shown in Fig. 4(a) as four green circles and three blue circles labeled as "set 2."
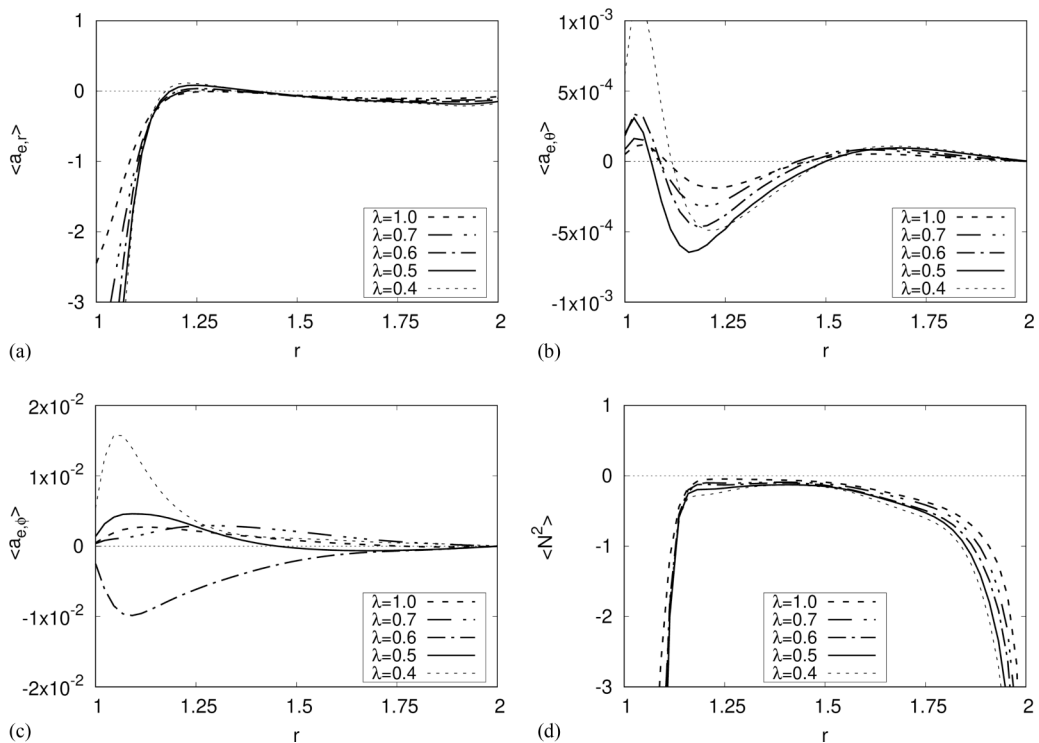
FIG. 8. Averaged (a) radial component of dielectrophoretic acceleration, (b) meridional component of dielectrophoretic acceleration, (c) azimuthal component of dielectrophoretic acceleration, and (d) Brunt-Väisälä frequency for $\lambda < 1$ and $1.4 \times 10^4 < L < 2.4 \times 10^4$.

1. Thermal profile

The maximum of the mean temperature is found in the middle of the gap [see Fig. 9(a)] and shifted toward the outer shell located at $r = 1.5$ which represents a higher value than that of the conductive case $r_{max} = 4/3$. This shift was also observed in Zaussinger *et al.* [12] and can be explained by an "eroding" convective flow.

The observed thermal fluctuations [see Fig. 9(b)] in the outer gap region are higher than in the case of $\lambda < 1$. This leads to statistical outliers and therefore high values in the kurtosis. This is well observed for the case where $-1 < S \lesssim 0$ and $2 < K \lesssim 3$ and is indicated in Fig. 9(c) and 9(d). In contrast to the cases with low internal heating, the skewness is negative in the lower gap region, but showed a steeper ascent for $r < 1.75$. A closer look to the three-dimensional temperature field reveals the negative sign of S and shows strong pointwise down-welling plumes. Four distinct pointwise plumes are highlighted and occurred as double-eye structures as shown in Fig. 10(b) where white rectangles highlight these structures. However, columnar cells are not observed for $L > 5 \times 10^4$ which is a result of the internal heating process. The columnar cells vanish by the convective flux that reversed the sign of the dielectrophoretic acceleration.

2. Stability and N^2

For $\lambda \geqslant 5.0$ the dielectrophoretic acceleration is positive between $r = 1.1$ and $r = 1.4$ [see Fig. 11(a)]. However, near the outer boundary, the dielectrophoretic acceleration is small or zero. The inversion of the sign of the dielectrophoretic acceleration would lead to a separation of the flow into two unstable layers separated by a stable, diffusive interface. However, layering is not observed in the numerical simulations. This can be explained by the buoyancy force in the gap.
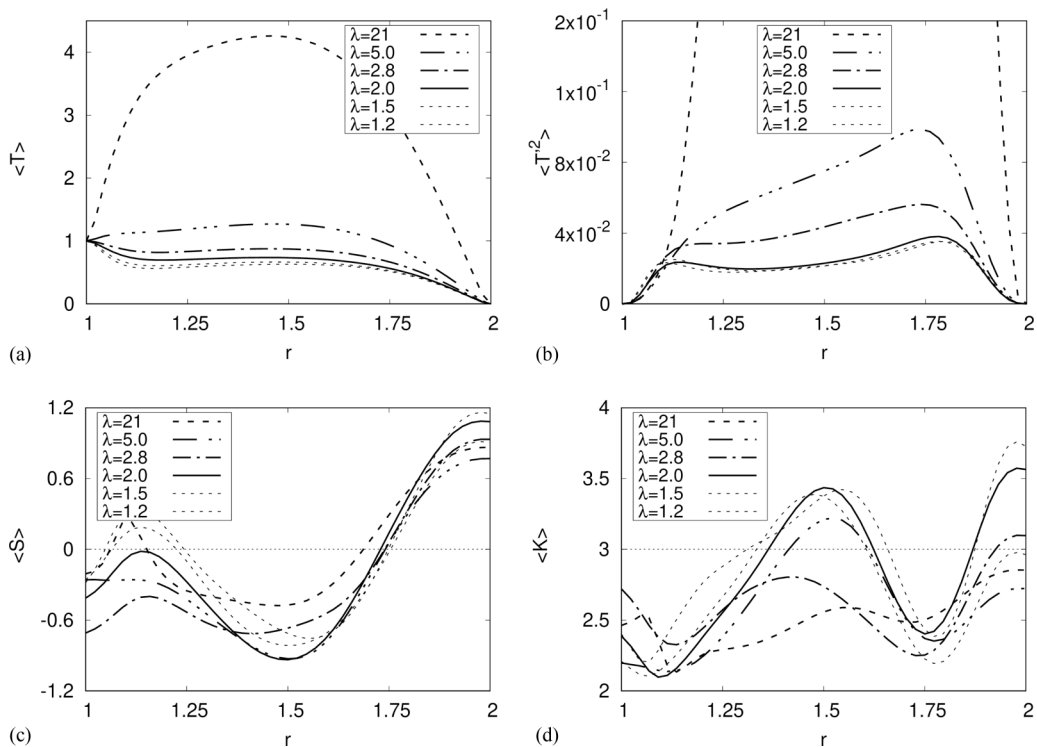
FIG. 9. Averaged (a) temperature, (b) temperature variance, (c) skewness of temperature, and (d) kurtosis of temperature for $\lambda \geqslant 1$ and $2.0 \times 10^3 < L < 3.5 \times 10^4$.

The dielectrophoretic acceleration is at least an order of magnitude higher at the inner shell than in the bulk or in the upper shell. This destabilized the diffusive interface where the dielectrophoretic acceleration changes sign and is able to form a convection cell which fills the entire gap. The
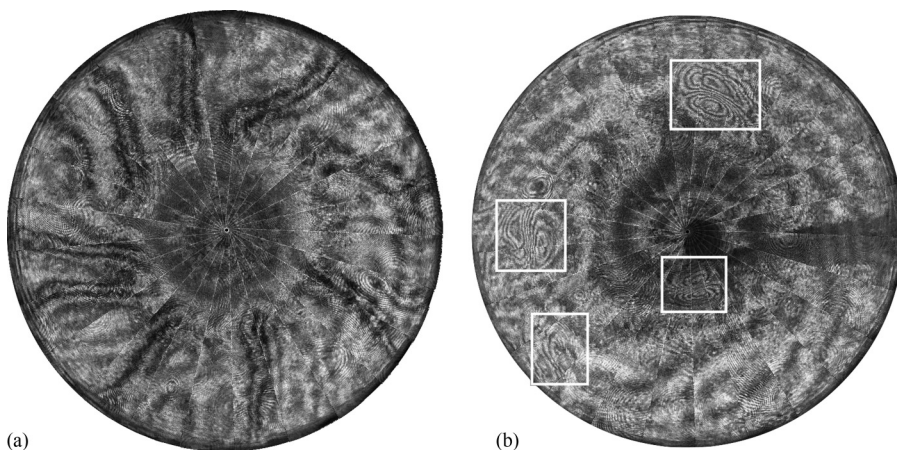

FIG. 10. Interferograms of the GeoFlow experiment with the North Pole at the center of the circle: (a) Remnants of columnar cells for $L = 2.4 \times 10^4$ and $\lambda = 0.7$. (b) Equatorial, pointwise plumes for $L = 6000$ and $\lambda = 60$ with highlighted structures after postprocessing.
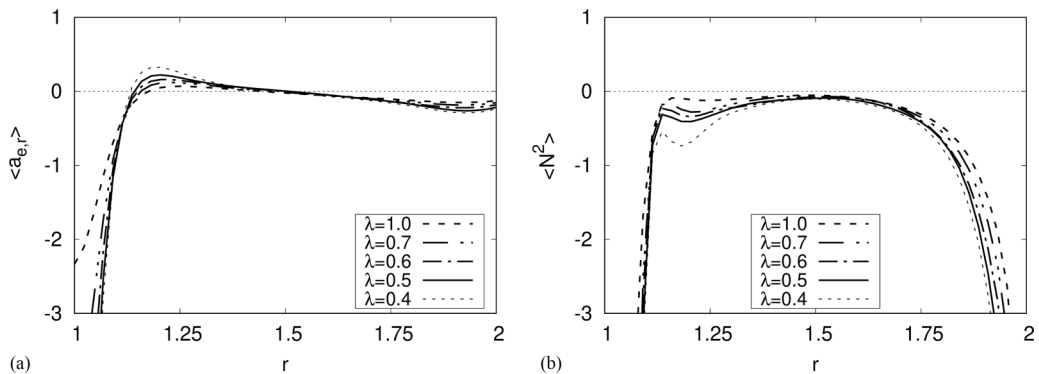
FIG. 11. Averaged (a) radial component of dielectrophoretic acceleration and (b) Brunt-Väisälä frequency for $\lambda \geqslant 1$ and $2.0 \times 10^3 < L < 3.5 \times 10^4$.

negative sign of the BV frequency over the entire gap confirms this and is shown in Fig. 11. The horizontal components of the dielectrophoretic acceleration are of comparable magnitude to those in the case of $\lambda < 1$ and do not contribute to the flow.

VI. DISCUSSION AND CONCLUDING REMARKS

In contrast to other spherical shell experiments (see Refs. [51,52]) the GeoFlow experiment provides a platform for investigating convection triggered by the dielectrophoretic effect with two heating sources; dielectric heating ($\lambda > 1$) caused by a fast alternating electric field and a temperature difference across the gap ($\lambda < 1$). Furthermore, it is the first study of rotating convection which includes both heating sources and a micro-gravity environment.

We predicted a separation of the flow into two layers in the absence of Earth's gravity. However, we were unable to find evidence of stable flow separation in the experiments or numerical simulations. One reason might be the electric buoyancy force which supports rapid mixing over the entire gap.

Internal heating in rotating RB systems was studied numerically, e.g., by Zhang and Busse [53]. They showed columnar convection for $Pr > 10$ and $Ek < 10^{-3}$, a parameter regime that coincides well with the above-presented results, although a temperature difference ΔT was not included in their work. A direct comparison with their results was difficult as the underlying governing equations differ in many aspects, e.g., the thermoelectric feedback or the centrifugal force term. However, a valid expression of the Taylor-Proudman theorem for the EHD model and columnar cells in the weakly nonlinear regime was found. The case of pure internal heating was analyzed by, e.g., Simitev and Busse [54] and showed results consistent with those found in the GeoFlow experiments in terms of spiral and overlapped columnar convection cells in the weakly nonlinear regime. Deschamps *et al.* [55] investigated volumetrically heated spherical gap convection in the nonrotating case. Numerical simulations showed steep down-welling thermal plumes and broad upwelling regions which agree with the GeoFlow experiments for $\lambda \gg 1$ in the transient regime.

The statistical evaluation showed that the EHD convection in the spherical gap can be described by the quasinormal approximation. Results provided good agreement to studies in the RB cell by Emran and Schumacher [56] where the first four statistical moments showed the same behavior in the plane geometry.

The most limiting feature of the GeoFlow experiment is its inaccessibility regarding visual measurement techniques. Due to safety and weight reasons, it was not possible to use tracer particles or larger adaption optics. Even though the interferograms showed only a projection of the thermal structure it was possible to extract basic properties of the convective flow. The onset of convection and generic convective patterns in the interferometry were compared with the linear stability

analysis and the regimes as defined in Gastine *et al.* [43]. The pointwise plume regime for $\lambda \gg 1$ where internal heating dominates over the centrifugal force was a limiting case in Zaussinger *et al.* [12]. In a first attempt, velocity and drift rates were determined by a machine learning algorithm. However, numerical simulations and measured velocities differed by up to a factor of four. In the future, it is planned to increase the number of measurement points to lower the statistical uncertainty.

Bifurcations and hysteresis effects in the rotating spherical gap were investigated by Feudel *et al.* [57] and Feudel *et al.* [58], respectively. Unfortunately, these effects cannot be confirmed with the experimental points of the GeoFlow IIc mission. The time scales of these experiments were only in the range of a few minutes. However, the GeoFlow IIb mission provided several studies with an experimental time of up to four hours. This data could be used in the future to investigate the above-mentioned bifurcations and hysteresis effects.

The GeoFlow experiment was performed at two reference temperatures, namely 293 K and 303.5 K. This experimental setup resulted in two Prandtl numbers, four Ekman numbers and ten Froude numbers. Each dimensionless value varied between its minimum and maximum by a factor of 1.41, 2.88, and 53, respectively. Differences were mainly found in the onset of convection and the wave numbers of the observed columnar cells. The wave numbers of the columnar cells in the GeoFlow experiment coincide with RB results (see Refs. [43,59]). However, no structural differences between the sets of four different Ekman numbers were found. The influence of the Froude number was not investigated. The complex interaction of all forces made it difficult to focus on this single influence. The weakly rotating case, Ek ~ 1, was not included in this study and will be used for future investigations. For the weakly rotating case, regular geometric structures such as tetrahedrons and octahedrons are expected [25]. Unfortunately, the GeoFlow experimental container was withdrawn from service aboard the ISS in December 2018 which makes a resumption of experimental work impossible.

The launch of the follow-up experiment AtmoFlow is planned for 2024. This experiment is designed to investigate atmospheric-like fluid flows [26].

APPENDIX: DERIVATION OF DIMENSIONLESS THERMOEHD EQUATIONS

We use the OBA for permittivity ϵ and the identity $\nabla(\epsilon|\mathbf{E}|^2) = \epsilon\nabla|\mathbf{E}|^2 + |\mathbf{E}|^2\nabla\epsilon$, to rewrite the dielectrophoretic force $\mathbf{F}_{\mathrm{DEP}}$ as

$$\mathbf{F}_{\mathrm{DEP}} = -\tfrac{1}{2}|\mathbf{E}|^2\nabla\epsilon = \tfrac{1}{2}\nabla[|\mathbf{E}|^2\epsilon_r\epsilon_0 e(T - T_0)] - \tfrac{1}{2}\epsilon_r\epsilon_0 e(T - T_0)\nabla|\mathbf{E}|^2, \tag{A1}$$

where the first term on the far-right-hand side is a gradient force and is included in the pressure gradient. The remaining term can be written as a electrical thermal buoyancy force, $\mathbf{F} = -\rho_0\alpha\,(T - T_0)\,\mathbf{g}_{\mathrm{e}}$ with

$$\mathbf{g}_{\mathrm{e}} = \frac{e}{\rho_0\alpha}\nabla\left(\frac{\epsilon_0\epsilon_r|\mathbf{E}|^2}{2}\right). \tag{A2}$$

This term is known as the *electric gravity* which represents a mean acceleration omitting spatial variations in the permittivity. Hence, $\mathbf{g}_{\mathrm{e}}$ alone is not suitable for the analysis of buoyancy related phenomena. In this study, the corresponding *dielectrophoretic acceleration* $\mathbf{a}_{\mathrm{e}} = \mathbf{F}_{\mathrm{DEP}}/\rho_0$ is instead

used which counts for all spatial variations of the permittivity and the temperature. This includes the consideration of the sign change of the dielectrophoretic acceleration under certain conditions which will also change the sign of the buoyancy term. A comparable approach is used by Mutabazi *et al.* [28] where the electric gravity is split into a base state and a fluctuating part.

Since the electric field has to fulfill the Gauss equation $\nabla \cdot (\epsilon \mathbf{E}) = 0$ or rather the dimensionless formulation Eq. (A3), it is split into two parts and calculated via the gradient of electric potential $\mathbf{\Phi}$,

$$\nabla \cdot \left[(\epsilon_0 \epsilon_r - eT^* \Delta T) \frac{V_{\mathrm{rms}}}{d} \mathbf{E}^* \right] = 0, \tag{A3}$$

$$\mathbf{E}^* = \mathbf{E}_0^*(r^*) + \mathbf{E}_1^*(r^*, \theta, \varphi), \tag{A4}$$

$$\mathbf{E}_0^*(r^*) = -\nabla \Phi_0^*(r^*), \quad \mathbf{E}_1^*(r^*, \theta, \varphi) = -\nabla \Phi_1^*(r^*, \theta, \varphi). \tag{A5}$$

where poloidal and toroidal angles are denoted by θ and φ, respectively. Thus, the field $\mathbf{E}_0^*(r^*)$ satisfies $\nabla \cdot \mathbf{E}_0^*(r^*) = 0$ which can be calculated analytically

$$\mathbf{E}_0^*(r^*) = \frac{1}{\sqrt{\Gamma}} \frac{1}{r^{*2}} \mathbf{e}_{r^*}, \tag{A6}$$

where $\Gamma = (1 - \eta)^4 / \eta^2$ is a geometrical factor for the spherical shell and $\eta = R_{\mathrm{in}}/R_{\mathrm{out}}$ is the radius ratio. The electric potential is calculated via

$$\Delta \Phi_1^* = \frac{C_E \, \Gamma \, L}{1 - C_E \, \Gamma \, L \, T^*} \nabla T^* \cdot [\nabla \Phi_0^*(r) + \nabla \Phi_1^*(r, \theta, \varphi)], \tag{A7}$$

with the dielectric loss parameter $C_T = 4\pi f \epsilon_0^2 \epsilon_r^2 \tan \delta V_{\mathrm{rms}}^4 / (c_p \rho^2 \nu \kappa)$ and the convective parameter $C_E = \rho \nu \kappa / (2 \epsilon_0 \epsilon_r V_{\mathrm{rms}}^2)$.

For $|\mathbf{E}_1^*| \ll |\mathbf{E}_0^*|$ [cf. Figs. 8(a)–8(c) where the horizontal components of the dielectrophoretic acceleration are three order of magnitudes smaller than the radial component] the Navier-Stokes equation and the temperature equation read,

$$\mathrm{Pr}^{-1} \left[\frac{\partial \mathbf{u}^*}{\partial t^*} + (\mathbf{u}^* \cdot \nabla) \mathbf{u}^* \right] = -\mathrm{Pr}^{-1} \nabla p^* + \nabla^2 \mathbf{u}^* + B \cdot L \cdot T^* \cdot \frac{1}{r^{*5}} \mathbf{e}_r - \mathrm{Ek}^{-1} \mathbf{e}_z \times \mathbf{u}^*$$
$$+ L \cdot \mathrm{Fr} \cdot T^* r^* \sin \theta \, \mathbf{s} \tag{A8}$$

and

$$\frac{\partial T^*}{\partial t^*} + (\mathbf{u}^* \cdot \nabla) T^* = \nabla^2 T^* + \frac{C_T}{B \, \Gamma^2 \, L} \frac{1}{r^{*4}}, \tag{A9}$$

respectively. Apart from the internal heating term and the geometrical aspects, this set of equations is identical with the governing equations presented in Feudel *et al.* [25] [Eq.(1a)–(1c)] and for the rotating case shown by Curbelo *et al.* [35] [Eqs. (1) and (2)]. This model is not suitable for describing pure internal heating. For completeness, we refer to Travnikov *et al.* [60].

---

[1] S. A. Fagents, Considerations for effusive cryovolcanism on Europa: The post-Galileo perspective, J. Geophys. Res.: Planets **108**, 5139 (2003).

[2] T. Lay, J. Hernlund, and B. A. Buffett, Core–mantle boundary heat flow, Nat. Geosci. **1**, 25 (2008).

[3] S. E. Smrekar and C. Sotin, Constraints on mantle plumes on Venus: Implications for volatile history, Icarus **217**, 510 (2012).

[4] M. Ogawa, Mantle convection: A review, Fluid Dyn. Res. **40**, 379 (2008).

[5] G. Schubert and D. Bercovivi, *Treatise on Geophysics*, Vol. 7, Mantle Dynamics (Elsevier, Amsterdam, 2009).

[6] D. J. Tritton, Internally heated convection in the atmosphere of Venus and in the laboratory, Nature **257**, 110 (1975).

[7] Y. Tasaka, Y. Kudoh, Y. Takeda, and T. Yanagisawa, Experimental investigation of natural convection induced by internal heat generation, J. Phys.: Conf. Ser. **14**, 168 (2005).

[8] J. Takahashi, Y. Tasaka, Y. Murai, Y. Takeda, and T. Yanagisawa, Experimental study of cell pattern formation induced by internal heat sources in a horizontal fluid layer, Int. J. Heat Mass Transf. **53**, 1483 (2010).

[9] A. Limare, K. Vilella, E. Di Giuseppe, C. G. Farnetani, E. Kaminski, E. Surducan, V. Surducan, C. Neamtu, L. Fourel, and C. Jaupart, Microwave-heating laboratory experiments for planetary mantle convection, J. Fluid Mech. **777**, 50 (2015).

[10] L. Fourel, A. Limare, C. Jaupart, E. Surducan, C. G. Farnetani, E. C. Kaminski, C. Neamtu, and V. Surducan, The Earth's mantle in a microwave oven: Thermal convection driven by a heterogeneous distribution of heat sources, Exp. Fluids **58**, 90 (2017).

[11] E. Kaminski and M. Javoy, A two-stage scenario for the formation of the earth's mantle and core, Earth Planet. Sci. Lett. **365**, 97 (2013).

[12] F. Zaussinger, P. Haun, M. Neben, T. Seelig, V. Travnikov, C. Egbers, H. Yoshikawa, and I. Mutabazi, Dielectrically driven convection in spherical gap geometry, Phys. Rev. Fluids **3**, 093501 (2018).

[13] F. Zaussinger, A. Krebs, V. Travnikov, and Ch. Egbers, Recognition and tracking of convective flow patterns using Wollaston shearing interferometry, Adv. Space Res. **60**, 1327 (2017).

[14] F. Kupka and H. Muthsam, Modelling of stellar convection, Living Rev. Comput. Astrophys. **3**, 1 (2017).

[15] C. Jaupart, S. Labrosse, F. Lucazeau, and J.-C. Mareschal, 7.06 - Temperatures, heat, and energy in the mantle of the Earth, in *Treatise on Geophysics* (2nd ed.), edited by Gerald Schubert (Elsevier, Oxford, 2015), pp. 223–270.

[16] B. Travis and P. Olson, Convection with internal heat sources and thermal turbulence in the earth's mantle, Geophys. J. Int. **118**, 1 (1994).

[17] K. Vilella and F. Deschamps, Temperature and heat flux scaling laws for isoviscous, infinite Prandtl number mixed heating convection, Geophys. J. Int. **214**, 265 (2018).

[18] P. H. Roberts, Electrohydrodynamic convection, Q. J. Mech. Appl. Math. **22**, 211 (1969).

[19] R. J. Turnbull, Effect of dielectrophoretic forces on the bénard instability, Phys. Fluids **12**, 1809 (1969).

[20] P. J. Stiles, Electro-thermal convection in dielectric liquids, Chem. Phys. Lett. **179**, 311 (1991).

[21] P. J. Stiles, F. Lin, and P. J. Blennerhassett, Convective heat transfer through polarized dielectric liquids, Phys. Fluids A **5**, 3273 (1993).

[22] B. L. Smorodin, The effect of an alternating electric field on the liquid dielectric convection in a horizontal capacitor, Tech. Phys. Lett. **27**, 1062 (2001).

[23] H. N. Yoshikawa, M. Tadie Fogaing, O. Crumeyrolle, and I. Mutabazi, Dielectrophoretic rayleigh-bénard convection under microgravity conditions, Phys. Rev. E **87**, 043003 (2013).

[24] M. T. Fogaing, H. N. Yoshikawa, O. Crumeyrolle, and I. Mutabazi, Heat transfer in the thermo-electro-hydrodynamic convection under microgravity conditions, Eur. Phys. J. E **37**, 1 (2014).

[25] F. Feudel, K. Bergemann, L. S. Tuckerman, C. Egbers, B. Futterer, M. Gellert, and R. Hollerbach, Convection patterns in a spherical fluid shell, Phys. Rev. E **83**, 046304 (2011).

[26] F. Zaussinger, P. Canfield, A. Froitzheim, V. Travnikov, P. Haun, M. Meier, A. Meyer, P. Heintzmann, T. Driebe, and Ch. Egbers, AtmoFlow—Investigation of atmospheric-like fluid flows under microgravity conditions, Microgav. Sci. Technol. **31**, 569 (2019).

[27] C. Egbers, W. Beyer, A. Bonhage, R. Hollerbach, and P. Beltrame, The GeoFlow experiment on ISS (Part I): Experimental preparation and design of laboratory testing hardware, Adv. Space Res. **32**, 171 (2003), Gravitational effects in physico-chemical processes.

[28] I. Mutabazi, H. N Yoshikawa, M. T. Fogaing, V. Travnikov, O. Crumeyrolle, B. Futterer, and C. Egbers, Thermo-electro-hydrodynamic convection under microgravity: A review, Fluid Dyn. Res. **48**, 061413 (2016).

[29] K. G. Ayappa, S. Brandon, J. J. Derby, H. T. Davis, and E. A. Davis, Microwave driven convection in a square cavity, AIChE J. **40**, 1268 (1994).

[30] R. Cherbański and L. Rudniak, Modelling of microwave heating of water in a monomode applicator—Influence of operating conditions, Int. J. Therm. Sci. **74**, 214 (2013).

[31] A. Castellanos, *Electrohydrodynamics*, Vol. CISM courses and lectures-380 (Springer-Verlag Wien GmbH, Wien, 1998).

[32] M. Zahn, Derivation of the korteweg-helmholtz electric and magnetic force densities including electrostriction and magnetostriction from the quasistatic poynting's theorems, in *Proceedings of the 2006 IEEE Conference on Electrical Insulation and Dielectric Phenomena* (IEEE, Los Alamitos, CA, 2006), pp. 186–189.

[33] J. R. Melcher, *Continuum Clectromechanics*, (MIT Press, Cambridge, MA, 1981).

[34] C. Gabriel, S. Gabriel, E. H. Grant, E. H. Grant, B. S. J. Halstead, and D. Michael P. Mingos, Dielectric parameters relevant to microwave dielectric heating, Chem. Soc. Rev. **27**, 213 (1998).

[35] J. Curbelo, J. M. Lopez, A. M. Mancho, and F. Marques, Confined rotating convection with large prandtl number: Centrifugal effects on wall modes, Phys. Rev. E **89**, 013019 (2014).

[36] O. Dupont, T. Dewandre, J.-L. Dewandel, and D. Claessens, The optical diagnostics of the fluid science laboratory, in *Proceedings of the 5th International Conference on Space Optics, Toulouse, France*, edited by B. Warmbein (ESA Publications Division, Netherlands, 2004), pp. 463–470.

[37] R. Hollerbach, A spectral solution of the magneto-convection equations in spherical geometry, Int. J. Numer. Methods Fluids **32**, 773 (2000).

[38] V. Travnikov, C. Egbers, and R. Hollerbach, The Geoflow-experiment on ISS (Part II): Numerical simulation, Adv. Space Res. **32**, 181 (2003).

[39] W.-W. Kim and S. Menon, A new dynamic one-equation subgrid-scale model for large eddy simulations, in *Proceedings of the 33rd Aerospace Sciences Meeting and Exhibit* (American Institute of Aeronautics and Astronautics, Reston, Virginia, 1995).

[40] F. Kupka, F. Zaussinger, and M. H. Montgomery, Mixing and overshooting in surface convection zones of DA white dwarfs: First results from ANTARES, Mon. Not. R. Astron. Soc. **474**, 4660 (2018).

[41] J. D. Scheel and J. Schumacher, Global and local statistics in turbulent convection at low prandtl numbers, J. Fluid Mech. **802**, 147 (2016).

[42] J. Curbelo and A. M. Mancho, Symmetry and plate-like convection in fluids with temperature-dependent viscosity, Phys. Fluids **26**, 016602 (2014).

[43] T. Gastine, J. Wicht, and J. Aubert, Scaling regimes in spherical shell rotating convection, J. Fluid Mech. **808**, 690 (2016).

[44] K. Zhang, Spiralling columnar convection in rapidly rotating spherical fluid shells, J. Fluid Mech. **236**, 535 (1992).

[45] F. H. Busse, Thermal instabilities in rapidly rotating systems, J. Fluid Mech. **44**, 441 (1970).

[46] See Supplemental Material at http://link.aps.org/supplemental/10.1103/PhysRevFluids.5.063502 for animation of columnar cells with $m = 4$.

[47] See Supplemental Material at http://link.aps.org/supplemental/10.1103/PhysRevFluids.5.063502 for animation of columnar cells with $m = 5$. .

[48] See Supplemental Material at http://link.aps.org/supplemental/10.1103/PhysRevFluids.5.063502 for animation of columnar cells with $m = 6$. .

[49] V. M. Gryanik, J. Hartmann, S. Raasch, and M. Schröter, A refinement of the millionshchikov quasi-normality hypothesis for convective boundary layer turbulence, J. Atmos. Sci. **62**, 2632 (2005).

[50] T. Gastine, J. Wicht, and J. M. Aurnou, Turbulent rayleigh–bénard convection in spherical shells, J. Fluid Mech. **778**, 721 (2015).

[51] F. H. Busse and C. R. Carrigan, Laboratory simulation of thermal convection in rotating planets and stars, Science **191**, 81 (1976).

[52] J. E. Hart, G. A. Glatzmaier, and J. Toomre, Space-laboratory and numerical simulations of thermal convection in a rotating hemispherical shell with radial gravity, J. Fluid Mech. **173**, 519 (1986).

[53] K.-K. Zhang and F. H. Busse, On the onset of convection in rotating spherical shells, Geophys. Astrophys. Fluid Dyn. **39**, 119 (1987).

[54] R. Simitev and F. H. Busse, Patterns of convection in rotating spherical shells, New J. Phys. **5**, 97 (2003).

[55] F. Deschamps, C. Yao, P. J. Tackley, and C. Sanchez-Valle, High rayleigh number thermal convection in volumetrically heated spherical shells, J. Geophys. Res.: Planets **117**, E09006 (2012).

[56] M. S. Emran and J. Schumacher, Fine-scale statistics of temperature and its derivatives in convective turbulence, J. Fluid Mech. **611**, 13 (2008).

[57] F. Feudel, L. S. Tuckerman, M. Gellert, and N. Seehafer, Bifurcations of rotating waves in rotating spherical shell convection, Phys. Rev. E **92**, 053015 (2015).

[58] F. Feudel, L. S. Tuckerman, M. Zaks, and R. Hollerbach, Hysteresis of dynamos in rotating spherical shell convection, Phys. Rev. Fluids **2**, 053902 (2017).

[59] P. H. Roberts, On the thermal instability of a rotating-fluid sphere containing heat sources, Philos. Trans. R. Soc. Lond. A **263**, 93 (1968).

[60] V. Travnikov, F. Zaussinger, P. Haun, and Ch. Egbers, Influence of the dielectrical heating on the convective flow in the radial force field, Phys. Rev. E **101**, 053106 (2020).